Indian J Phys (June 2015) 89(6):561–570
DOI 10.1007/s12648-014-0620-5

ORIGINAL PAPER

Enhanced electro-magnetic properties in $La_{0.7}Sr_{0.3}MnO_3/ZrO_2$ composites

A M Ahmed*, H F Mohamed, A K Diab, Abd El-Mo'ez A Mohamed, A E A Mazen and A M Mohamed

Department of Physics, Faculty of Science, Sohag University, Sohâg 82524, Egypt

Received: 06 August 2014 / Accepted: 29 October 2014 / Published online: 11 November 2014

Abstract: $(La_{0.7}Sr_{0.3}MnO_3)_{1-x}/(ZrO_2)_x$ ($x = 0.0$–0.150, step 0.025) composites have been prepared via solid state reaction process. The X-ray diffraction and scanning electron microscopic observations indicate that there are ZrO_2 grains separated from $La_{0.7}Sr_{0.3}MnO_3$ matrix. It has been found that the inclusion of ZrO_2 content decreases the conductivity, magnetization and metal–semiconductor transition, whereas it increases the low field magnetoresistance. Possible effects of grain boundaries on the low field magnetoresistance have been discussed. The small ZrO_2 grains are trapped between $La_{0.7}Sr_{0.3}MnO_3$ grains may be acting as a barrier for spin-polarized tunneling and enhance the low-field magnetoresistance.

Keywords: Colossal magnetoresistance; Electrical resistivity; DC magnetization

PACS Nos.: 75.47.Lx; 75.47.Gk; 72.80.Tm

1. Introduction

Hole-doped manganite perovskites of the type $La_{1-x}Sr_xMnO_3$, have attracted enormous interest in recent time due to the colossal magnetoresistance (CMR) effect [1–3]. Recently, enhanced low-field magnetoresistance (LFMR) or room temperature magnetoresistance (RTMR) properties have been successfully achieved for manganite composites by having grain boundaries material. The intrinsic colossal magnetoresistance (*i*CMR) effect [4], which is caused by double exchange (DE) mechanism [5], is usually found during a narrow temperature range near the Curie temperature (T_c) [6] and needs high magnetic field. This is not very appealing for practical application. Recently, another type of magnetoresistance (MR) has been found in polycrystalline manganites. This kind of MR is mainly dependent on the grain boundary properties and the spin-polarized tunneling of conduction electrons [7] and it usually occurs over a wide temperature range and at a low magnetic field. Hence, it's called as LFMR, which is associated with the spin-memory contribution to charge transport across the grain boundary (or interface) by modifying the microstructure of the manganites. There are some other extrinsic MR effects, such as grain boundary MR and spin-polarized transport MR [8, 9].

LFMR could be more useful for practical applications. In order to improve the LFMR, it is suggested that it is very useful to prepare the composites, composed of matrix and insulating inclusions. Examples can be typically found in ferromagnetic (FM)/insulator (*I*) type, such as $La_{0.7}Sr_{0.3}MnO_3/CeO_2$, $La_{0.7}Sr_{0.3}MnO_3/SrTiO_3$ and $La_{0.7}Sr_{0.3}MnO_3$/glass composites etc. The second oxide phase of composite acts as a spin-polarized tunneling barrier for the first oxide phase (manganite) [4–7].

The LFMR property is also affected by several factors as sintering temperature, impurity, complicated band structure, electron–electron, electron–magnon scattering, etc. The present work aims to study the electric and magnetic properties of composites, which is designed with ferromagnetic $La_{0.7}Sr_{0.3}MnO_3$ (LSMO) and insulating ZrO_2.

2. Experimental details

Samples in the composite series $(La_{0.7}Sr_{0.3}MnO_3)_{1-x}/(ZrO_2)_x$ with $x = 0.0$, 0.025 0.05, 0.075, 0.10, 0.125 and 0.15 wt%, were prepared in a required ratio by the conventional solid state reaction method. The starting chemicals La_2O_3, $SrCO_3$ and $MnCO_3$ were mixed in stoichiometric proportions to prepare the parent compound.

*Corresponding author, E-mail: fikry_99@yahoo.com

La_2O_3 was dehydrated at 873 K for 6 h. The mixture was ground for 6 h to ensure homogeneity and pressed into pellets under a pressure of 5 tons cm^{-2}. The pellets were calcined twice for 12 h at 1,273 K and then ground at the same conditions. The pellets were ground, mixed and subsequently sintered in air at 1,573 K for 48 h. The obtained LSMO powders with single-phase perovskite structure, were completely mixed with a high purity ZrO_2 powder according to the desired ratio $(La_{0.7}Sr_{0.3}MnO_3)_{1-x}/(ZrO_2)_x$ with x = 0.025, 0.05, 0.075, 0.10, 0.125 and 0.150 wt%. The resulting powders $(La_{0.7}Sr_{0.3}MnO_3)_{1-x}/(ZrO_2)_x$ were ground, pelletized at pressure of 5 tons cm^{-2} and then the sintering was repeated at 1,273 K for 24 h. The low sintering temperature was chosen to avoid inter-diffusion of LSMO and ZrO_2. The structural characterization was examined by X-ray diffraction at room temperature. Crystal structure and lattice parameters were refined by Rietveld method using FULLPROF program. The surface morphology was investigated by scanning electron microscopy (SEM Model JSM-6610LV). The electrical measurements under applied and without (zero) magnetic field were carried out by standard Van der-pauw technique in the temperature range 80–290 K [8–10]. MR, was then calculated from $MR = [\rho(H) - \rho(0)]/\rho(0)$, where $\rho(H)$ the resistivity measured under applied magnetic field equal to 0.6 T and $\rho(0)$ the resistivity measured in the absence of magnetic field.

The DC magnetization measurements were done using a vibrating sample magnetometer.

3. Results and discussion

The XRD patterns of composites (x = 0.0, 0.025, 0.05, 0.075, 0.10, 0.125 and 0.150 wt%) are plotted in Fig. 1. It is clear that they have two phases: one phase is rhombohedral LSMO and the other is cubic ZrO_2 [11]. In addition to, small peaks of impurity is also observed. The diffraction patterns also show the shift to higher angles with increasing Zr content except the sample of x = 0.10.

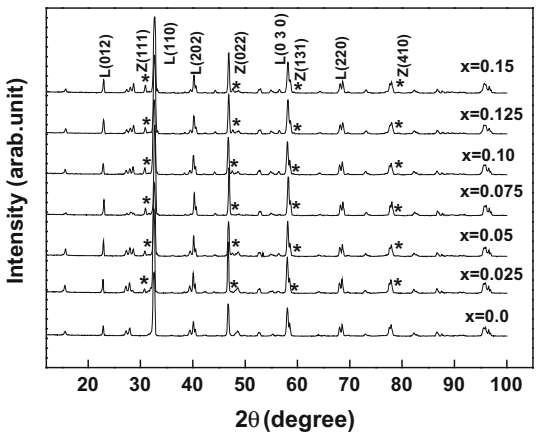

Fig. 1 X-ray patterns of $La_{0.7}Sr_{0.3}MnO_{1-x}/(ZrO_2)_x$ (x = 0.0, 0.025–0.15 %)

Rietveld analysis patterns, as shown in Fig. 2, have proved the crystallization of both parent and composite samples in the rhombohedral structure (space group $R\bar{3}c$). From Fig. 2(a)–2(c), we can see a small impurity of LaSrO and MnO and there are small peaks at $2\theta \approx 28.63$, 30.93, 47.56, 18.48 and 77.98 are related to ZrO_2. The intensity of theses peaks increases unsystematically with Zr content. We expect that a small portion of ZrO_2 may be dissolved in the Perovskite LSMO and replaced Mn atoms and the remaining amount forms as segregated grains on the grain boundaries and the surface of LSMO.

As seen in Table 1, the lattice constants and cell volume are slightly dependent on Zr content. This means that, Zr addition has a very weak effect, depending on the nonsequential dissolved small amount in the parent matrix compound.

Scanning electron microscopic picture of the powder of LSMO, $(LSMO)_{0.975}/(ZrO)_{0.025}$ and $(LSMO)_{0.85}/(ZrO)_{0.15}$ samples are shown in Fig. 3. Comparing between three images as in Fig. 3(a)–3(c), we observe that in sample Zr = 0 contains grains having ribbed shape (grey color), smooth surface and large size (4.3 μm). It is clear that the Fig. 3(b)–3(d), have a very small grains (ZrO_2-white color) spread on the surface of LSMO matrix and occupy interstitial sites on the grain boundaries. It is confirmed that no chemical reaction occurs between LSMO and ZrO_2 phases coexist. Besides the size of grain decreases with increasing Zr content. Figure 3(e), shows an analysis of Energy-dispersive X-ray spectroscopy of $Zr_{x=0.025}$ content. We observe that, the points on smooth surface (2, 3) have zero Zr and points 1 and 4 contain a small percentage of Zr elements.

Additionally, the large LSMO grains are randomly distributed and well surrounded by small ZrO_2 grains, which is in agreement with results of Lu et al. [12]. We can confirm no reaction between the LSMO and ZrO_2, which indicates that $(La_{0.7}Sr_{0.3}MnO_3)_{1-x}/(ZrO_2)_x$ composites contain two-phase mixed microstructure [11].

The temperature dependence of the resistivity for samples measured at zero field is shown in Fig. 4(a)–4(g). Generally, all samples show metal–semiconductor transition at a certain temperature T_{ms}. Moreover, the values of ρ(T) and T_{ms} are found to depend on the parameters of composition. From Fig. 4 and Table 2, we can see a decrease in T_{ms} and an increase in resistivity except for $x = 0.075$. The decrease of T_{ms} and the increase of resistivity can be interpreted as the decrease of the grain sizes occurs due to enhance of scattering center for conduction

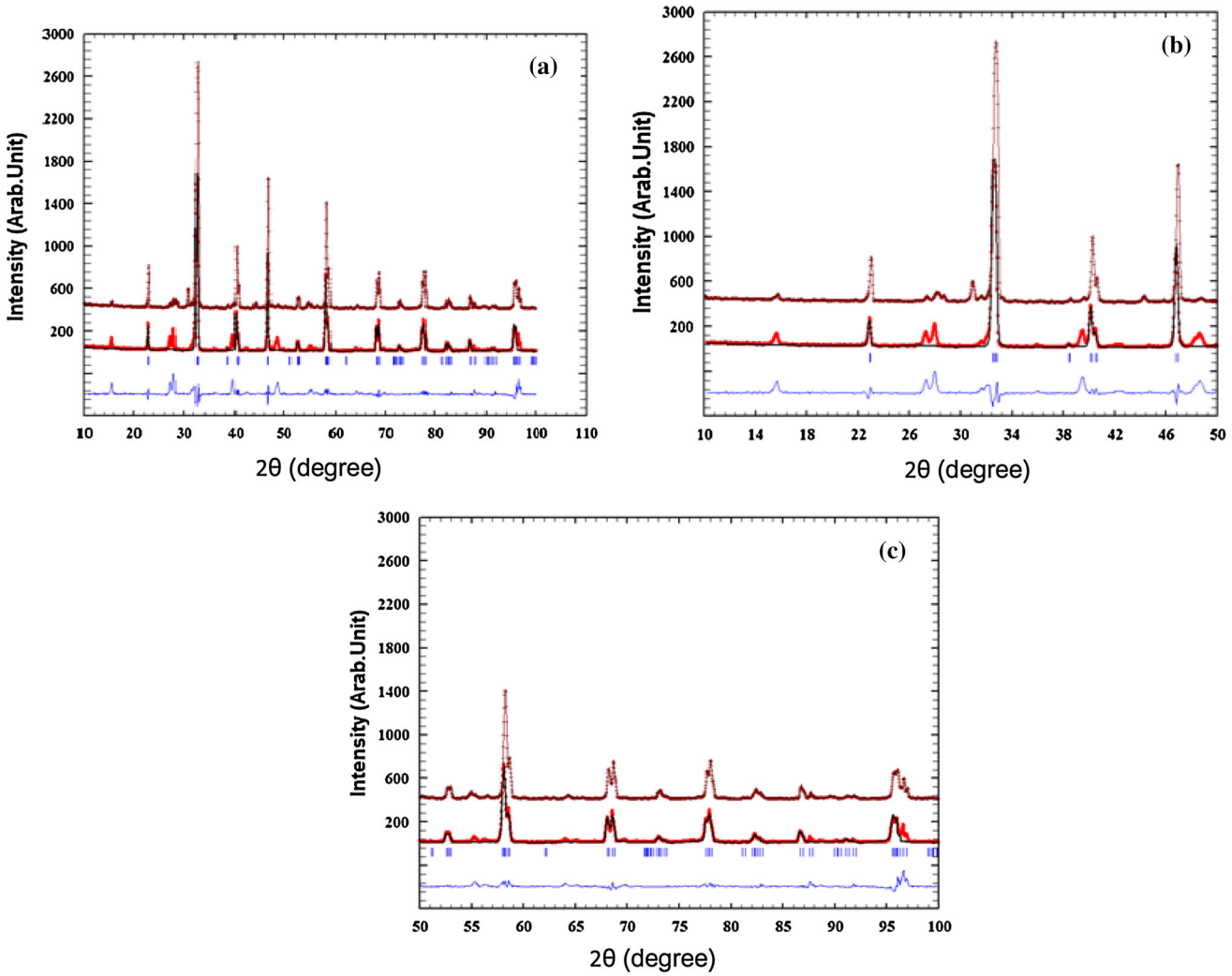

Fig. 2 (**a**) The Reitveld based calculated profile of $La_{0.7}Sr_{0.3}MnO_3$ (*middle curve*) and $(La_{0.7}Sr_{0.3}MnO_3)_{0.9}/(ZrO_2)_{0.10}$ (*upper curve*) at room temperature, where *blue marks* indicate Bragg reflections, the *brown dots* are the experimental data, *black line* is the theoretical calculations and the *blue line* is the difference between them, (**b**) a focus curves from 2θ = 10–50, (**c**) a focus curves from 2θ = 50°–100°. (Color figure online)

Table 1 Lattice parameters and cell volume of $(La_{0.7}Sr_{0.3}MnO_3)_{1-x}/(ZrO)_x$ (x = 0, 0.25, 0.05, 0.075, 0.1, 0.125 and 0.15)

x	a (Å)	c (Å)	V (Å)
0	5.5058	13.357	350.648
0.025	5.5022	13.3490	349.985
0.05	5.5054	13.3559	350.580
0.075	5.5062	13.3609	350.811
0.10	5.5045	13.3490	350.284
0.125	5.5079	13.3551	350.866
0.150	5.5077	13.3550	350.841

electron. For example, the occurrence of antiferromagnetic insulating region on the grain boundary may not modify the magnetic transition temperature but can make the metal-semiconducting transition shift to low temperature [13].

On the other hand, the resistivity $\rho(T)$ exhibits a discontinuity in low temperature range. This may be due to several scattering mechanisms [14]. Also our results are in agreement with these reported by Bearner et al. [15]

The electrical resistivity data in the semiconducting region are fitted to Mott's variable range hopping (VRH) and Mott and Davis's small polaron hopping (SPH) models [16, 17]. Mott's VRH model is valid at $\theta_D/2 \geq T \geq T_{ms}$, where the electrical resistivity obeys the expression in the three-dimensional hopping [18]

$$\rho(T) = \rho_0 \exp\left(\frac{T_0}{T}\right)^{1/4} \quad (1)$$

where T_0 is the Mott characteristic temperature, which can be expressed in the terms of density of states in the vicinity of Fermi energy, $N(E_F)$ and localization length "a" as follows:

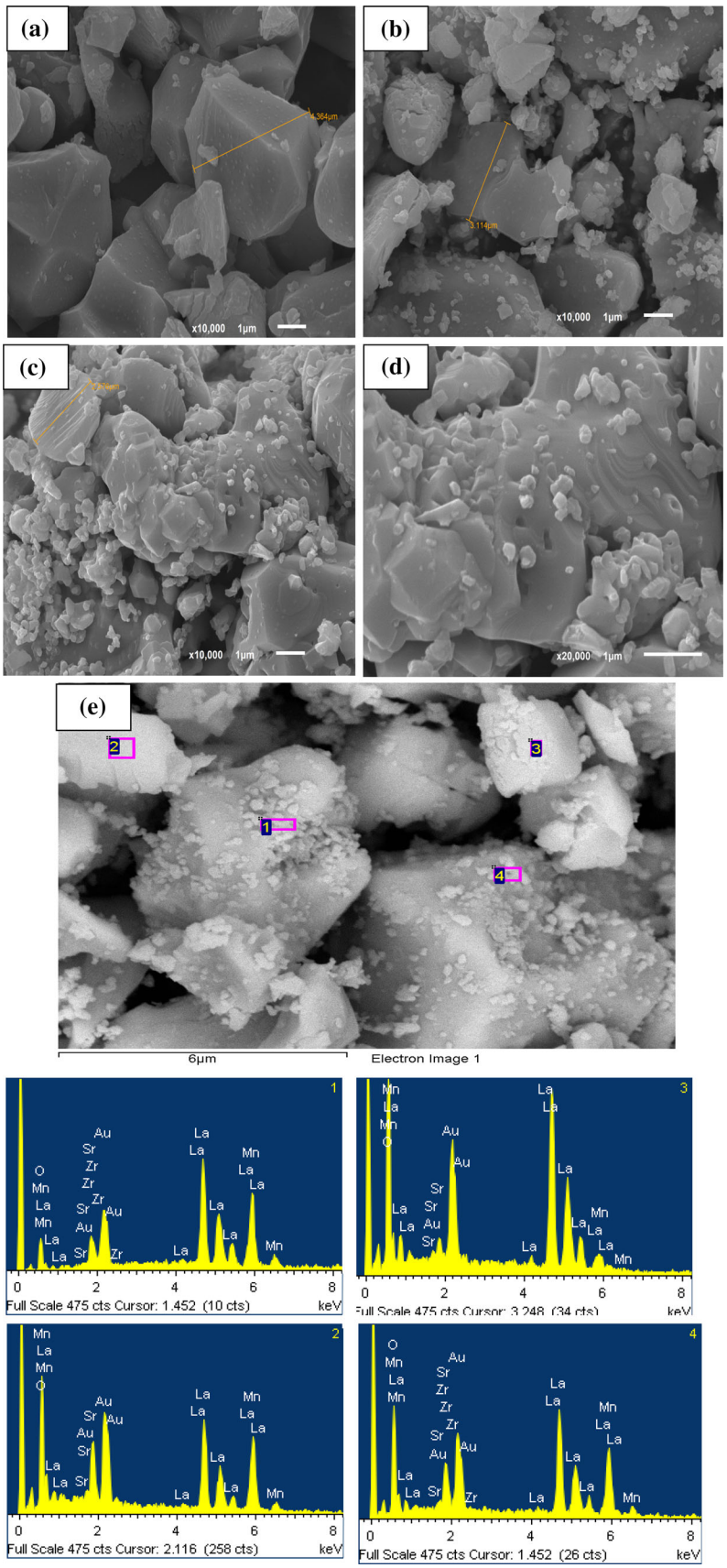

Fig. 3 SEM of $(La_{0.7}Sr_{0.3}MnO_3)_{1-x}/(ZrO_2)_x$ compound: (**a**) LSMO (x = 0.0), (**b**) x = 0.025, (**c**), (**d**) x = 0.15 and (**e**) EDAX of x = 0.025

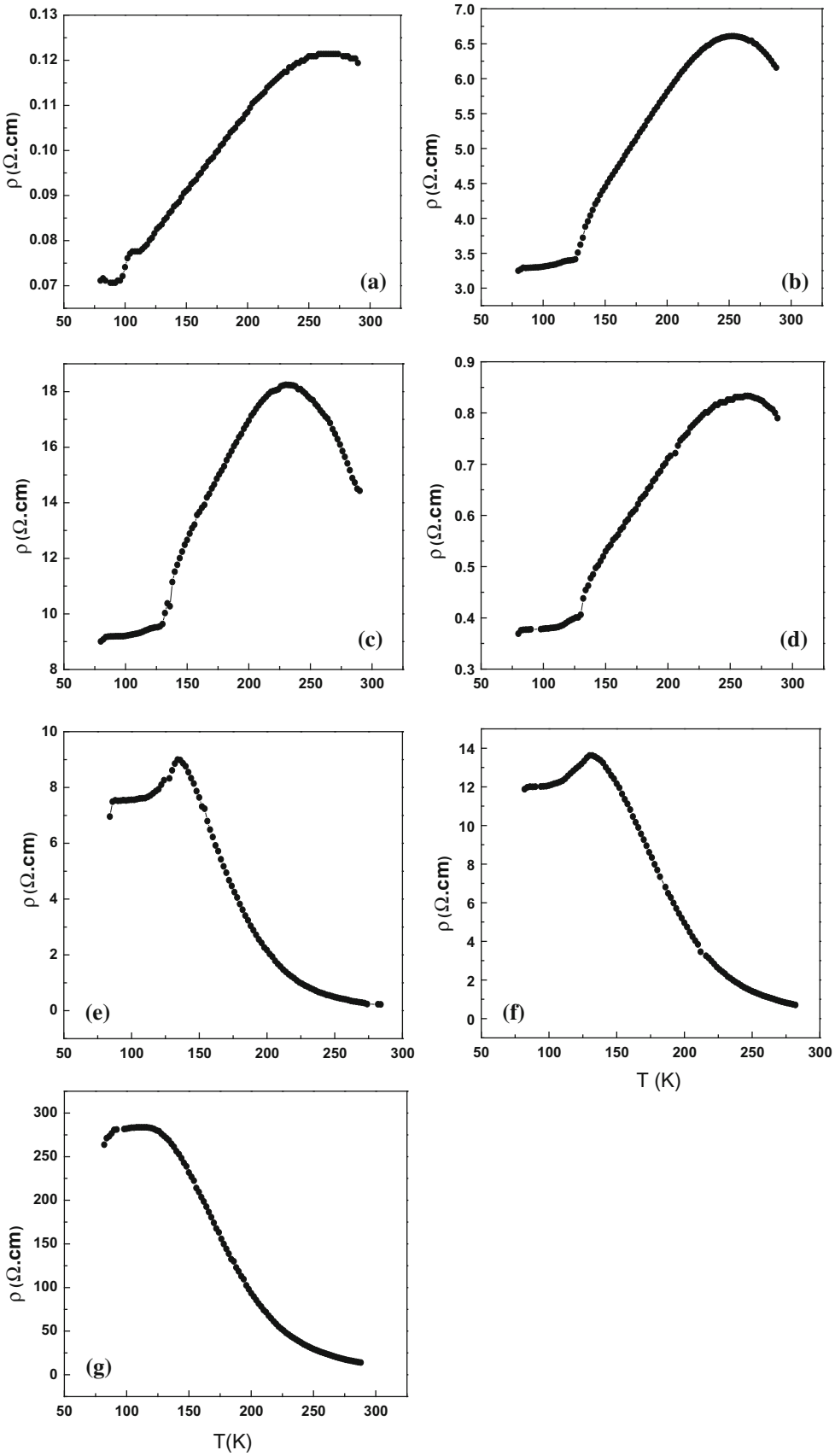

Fig. 4 Resistivity versus temperature for different compositions of LaSrMnO/ZrO_2, where (**a**) x = 0.0, (**b**) x = 0.025, (**c**) x = 0.05, (**d**) x = 0.075, (**e**) x = 0.10, (**f**) x = 0.125 and (**g**) x = 0.15

Table 2 The calculated parameters as function of Zr content

x	T_{ms} (K)	$E\rho$ (mev)	θ_D (K)	υ_{ph} (Hz) × 10^{-12}	$N(E_f)$ ev^{-1} cm^{-3}	W_H (mev)	J (mev)	H (mev)	γ	T_{c1} (K)	T_{c2} (K)
0	274	27.47	–	–	–	1.49	–	–	–	340	–
0.025	254	46.32	543.99	11.34	2.5×10^{24}	20.98	26.78	16.42	0.88	350	319
0.05	230	69.46	527.99	11	1.32×10^{23}	43.95	26.18	19.56	1.93	350	319
0.075	260	42.7	543.99	11.34	5.88×10^{24}	15.91	26.78	15.4	0.68	360	319
0.1	134	155.42	400	8.33	6.97×10^{19}	136.62	21.26	22.6	7.94	350	319
0.125	132	137.6	411	8.56	1.95×10^{20}	114.92	21.7	21.94	6.5	330	319
0.15	116	137.03	428	8.92	1.27×10^{20}	116.41	22.37	22.46	6.32	360	319

$$T_0 = \frac{18}{k_B N(E_f) a^3} \tag{2}$$

where T_0 is a constant (Mott characteristic temperature) $N(E_f)$ is the density of states near Fermi energy and a is the localization length, $a = 2.22$ nm^{-1} has been reported by Viret et al. [19]. The best fits experimental data to these models are shown in Fig. 5(a) and 5(b) for $x = 0.025$ and $x = 0.15$ respectively. These plots reveal that the data fits very well with the VRH model for the considered temperature range, suggesting the conduction being governed by the disorder induced localization of charge carriers. As could be seen in Table 2, generally there is a decrease in $N(E_F)$ due to the increase in resistivity.

The data have fitted to SPH in temperature range $T > \theta_D/2$ [20–22]. The SPH model gives:

$$\rho/T = \rho_\alpha \exp(E_\rho/k_B T) \tag{3}$$

where $\rho_\alpha = [k_B/\upsilon_{ph} N e^2 R^2 C(1-C)\exp(2\alpha R)]$, k_B is the Boltzmann constant and T is the absolute temperature, N is the number of ion sites per unit volume, $R \sim (1/N)^{1/3}$ is the average inter sites spacing, C is the fraction of sites occupied by polaron, α is the electron wave function decay constant, υ_{ph} is the optical phonon frequency estimated by the relation $h\upsilon_{ph} = k_B\theta_D$ and θ_D is the Debye temperature obtained from the temperature linearity of ln (ρ/T) versus $1/T$ above T_{ms} as shown in Fig. 6(a)–6(c) for $x = 0.0$, $x = 0.025$ and $x = 0.15$ respectively. The activation energy E_ρ is given by [23];

$$\begin{aligned} E_\rho &= W_H + W_D/2 \quad (\text{for } T > \theta_D/2) \\ &= W_D \quad (\text{for } T < \theta_D/4) \end{aligned} \tag{4}$$

where W_H is the polaron hopping energy and W_D is the disorder energy. The parameters are calculated and presented in Table 2. In Table 2 and Fig. 3, we observe that E_ρ is inversely proportional to the grain size, which means that with increasing grain size interconnectivity between grains increases cooperation of the conduction electrons to hop the neighboring sites [24]. The values $\theta_D/2$ is higher than T_{ms}, which highlights the width of VRH region between $\theta_D/2$ and T_{ms}. Phonon frequency υ_{ph} is similar to $\theta_D/2$ in behavior, while the parent sample has no θ_D, because of the temperature range above T_{ms} is fitted well as SPH model.

To determine either the hopping conduction in the adiabatic or non-adiabatic state, we have used Holstein's condition [25], which satisfies the following condition:

$$\begin{aligned} &J > H \ \text{(for adiabatic hopping condition)} \\ &J < H \ \text{(for non - adiabatic hopping condition)} \end{aligned} \tag{5}$$

$$\text{where, } H(T) = (2k_B T W_H/\pi)^{1/4}(h\upsilon_{ph}/\pi)^{1/2} \tag{6}$$

$$\text{and, } J(T) = 0.67 h\upsilon_{ph}(T/\theta_D)^{1/4} \tag{7}$$

By substituting the values of W_H, υ_{ph} and θ_D, the values of $H(T)$ and $J(T)$ at room temperature (290 K) are calculated and tabulated in Table 2. From this data, we have found that the samples $x \leq 0.075$ show the adiabatic hopping, while those with $x > 0.075$ exhibit the non-adiabatic hopping. Also for the samples with $0.025 \leq x \leq 0.075$ small polaron has been formed under condition $J > W_H/3$ [26], while in $x > 0.075$ a large polarn has been formed.

According to the relation $\gamma_p = 2W_H/h\upsilon_{ph}$ [25, 27], the factor γ_p, which gives an estimation of the e-phonon interaction could be determined. As seen in Table 2, the γ_P values are greater than 4 for $x \geq 0.10$, which according to Austin and Mott represent a strong electron–phonon interaction [28] and weak electron phonon interaction if it is less than 4 such as in $0.025 \leq x \leq 0.075$.

Temperature dependence of MR is shown in Fig. 7(a)–7(g), which show a peak at vicinity of T_{ms} transition and this observation is very important in industrial applications. In Fig. 7(a)–7(d), we observe that, there are dips for the samples $x = 0.0, 0.025, 0.05, 0.075, 0.125$ and 0.150 at $\sim$ 107, 131, 138, 121,125 and 122 K for Zr content respectively. This dip is followed by a broad peak, which is originated from the enhanced MR at low temperatures. On the other side, for the sample $x = 0.10$, as shown in Fig. 7(e), there is a sharp peak near T_{ms}, which is in agreement to doped manganites [29, 30]. We note that this dip shifts to high temperature by increasing Zr content up to 0.05. Thereafter,

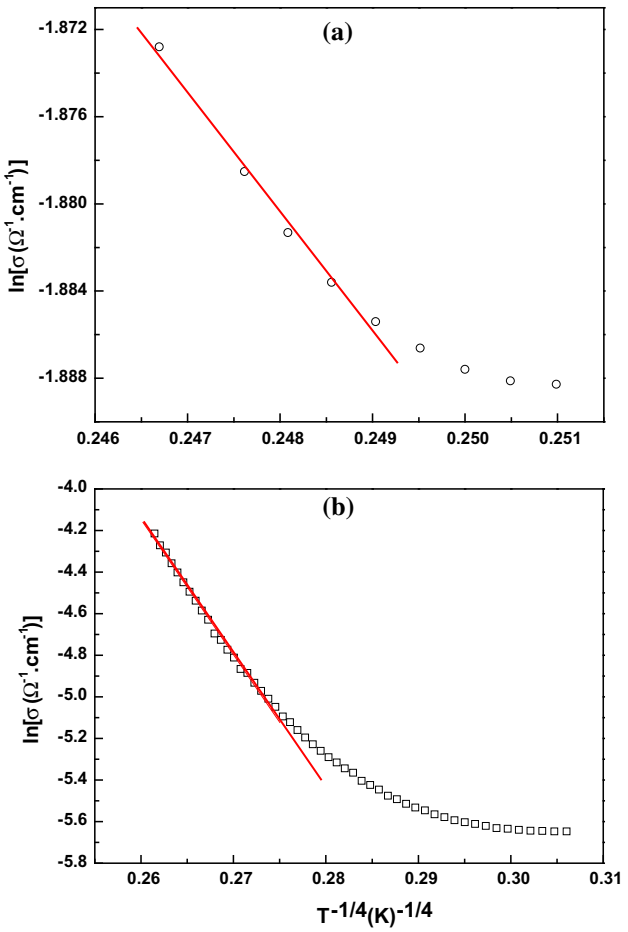

Fig. 5 ln(σ) versus $(T)^{-1/4}$ the *solid line* indicates the best fit to the (VRH) model between T_{ms} and $\theta_D/2$, (**a**) for x = 0.025 and (**b**) for x = 0.15

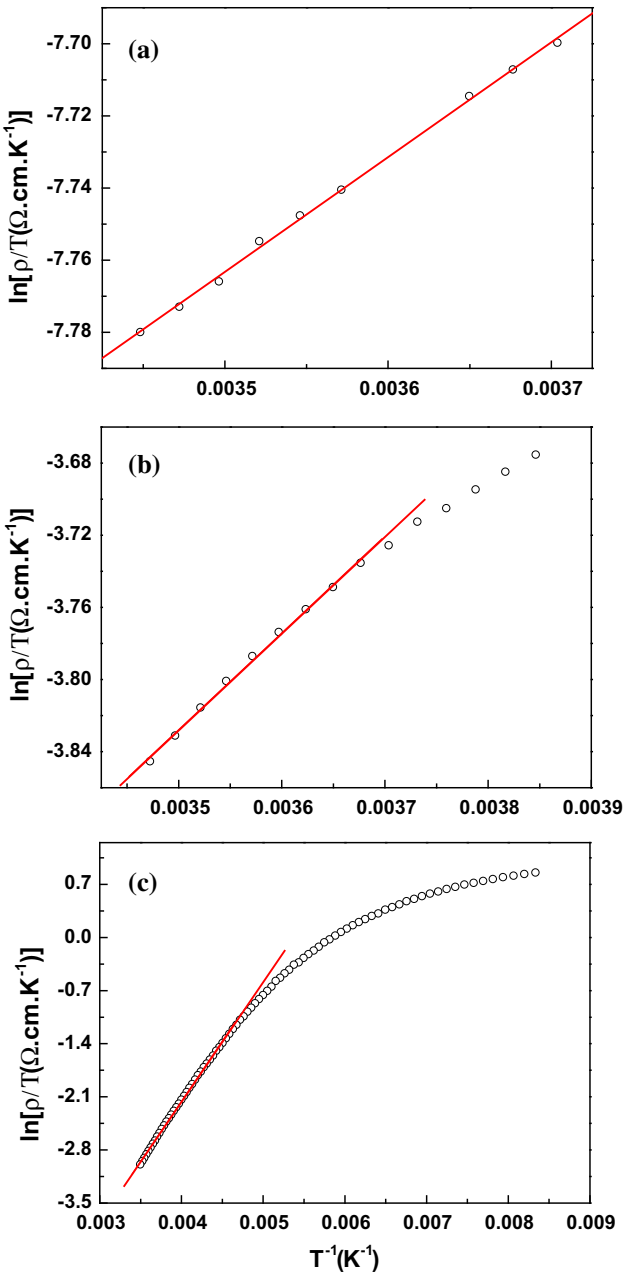

Fig. 6 ln(ρ/T) versus 1/T of the samples (**a**) for x = 0.0, (**b**) for x = 0.025 and (**c**) for x = 0.15, the *solid line* shows the best fitting with the small polaron hopping model of Mott

it changes non-sequentially. Below this dip, the MR increases with decreasing temperature monotonically. There are two different mechanisms causing maximum magnetoresistance; the first one is the intrinsic MR, which arises due to the suppression of spin fluctuations by aligning the spins on the application of magnetic field. This MR has highest value near the ferromagnetic transition temperature. The second one is the extrinsic MR, which arises due to inter-grain spin-polarized tunneling, across the grain boundaries (GBs) [31–33]. This MR contribution increases as the temperature decreases. As one can see in Fig. 7, both mechanisms are strongly effective in the present case. The change of MR sign is due to many factors like spin disorder, intergrain spin-polarized tunneling [33], nearly fully spin-polarized carriers tunneling through the insulating ZrO grains [31–34]. As a result, a positive MR appears [35, 36]. We point out that the best sample is $Zr_{x=\ 0.10}$, where MR reaches to 27 % at 123 K Table 3.

The DC magnetization measurements have been carried out over a temperature range of 100–420 K for samples in a magnetic field 100 Oe. The sample has been cooled from room temperature to 100 K in zero magnetic field and then the magnetization measurement $M\ (T)_{ZFC}$ has been carried out in the heating mode in applied magnetic field 100 Oe. Figure 8 shows the temperature dependence of DC magnetization *M (T)* curves. Generally, all samples show a magnetic transition from PM to FM at Curie temperature (T_c), which is corresponding to the peak of *dM/dT* versus temperature curves. We can see that there is a decrease in both magnetization and T_c with Zr content, which is a result of DE decrease due to the increase in the small

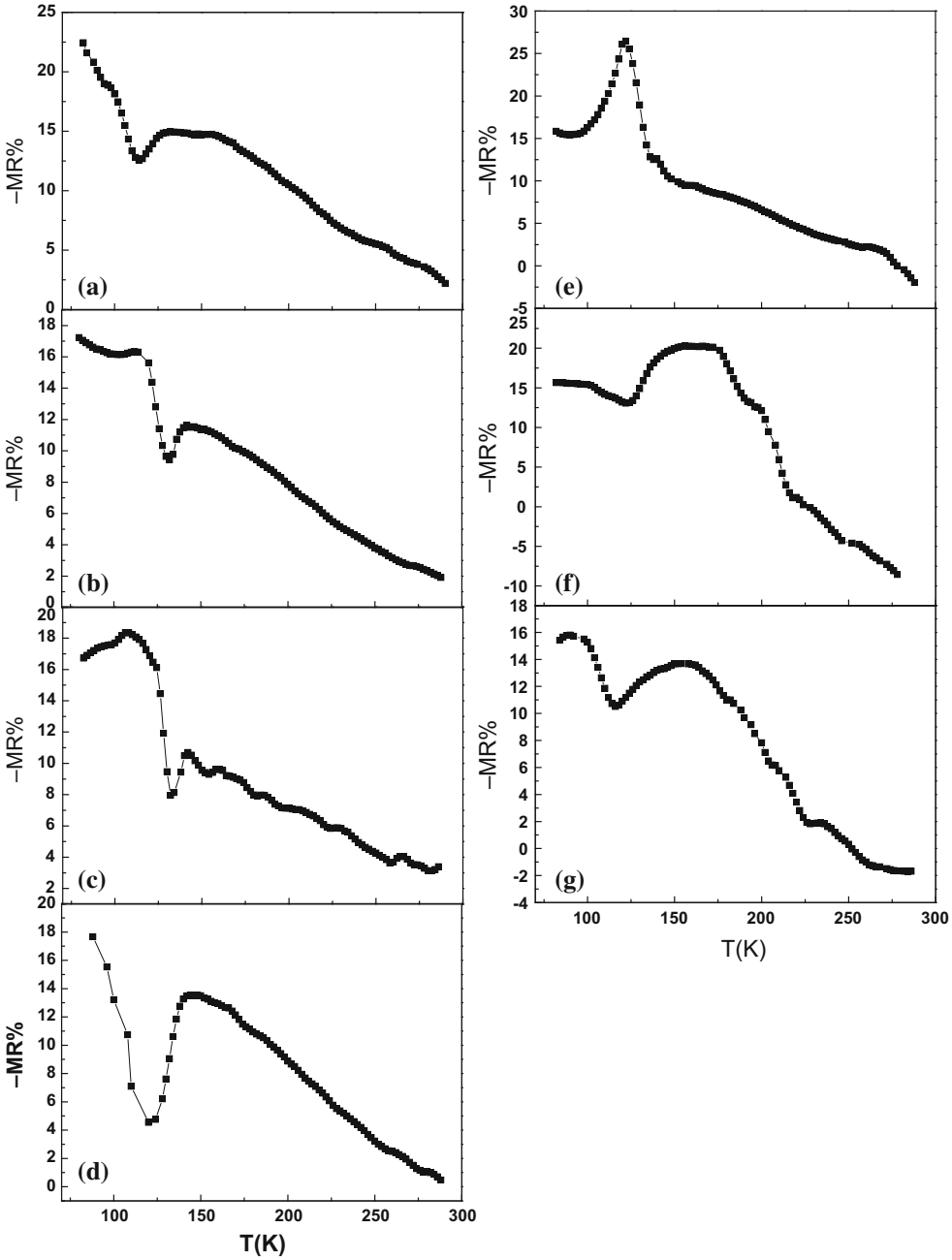

Fig. 7 −MR versus. Temperature for different compositions at 0.6 T. (**a**) x = 0.0, (**b**) x = 0.025, (**c**) x = 0.05, (**d**) x = 0.075, (**e**) x = 0.10, (**f**) x = 0.125 and (**g**) x = 0.15

Table 3 The maximum value −MR, and −MR value at RT

x	$-MR_{max}$ %, T (K)	T (K)	$-MR_{max}$ (RT)
0.0	23.80	80	2.6
0.025	17.4885	80	1.9877
0.05	18.417	108	3.378
0.075	17.385	80	2.948
0.1	27	123	−12.91
0.125	20.41	158	−9.15
0.15	16.1347	90	−1.7301

dissolved portion of Zr in LSMO lattice. With respect to $x = 0.075$, as the dissolved portion of Zr is very small or negligible. Thus, the increasing in magnetization and T_c is considered to be an expectable matter in agreement with electrical measurements. This drop at T_c is due to the magnetic anisotropy and also the mutual magnetic interaction between the domains. As we said previously, the possible cause for the decrease of T_{ms}, T_c and magnetization could be the doping effect of Zr ions into B sites of LSMO. Many experiments have shown that a small amount of doping element entering the B sites in the Perovskite

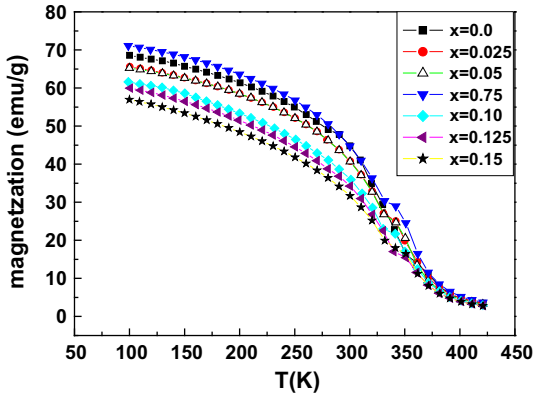

Fig. 8 Magnetization versus temperature for different compositions

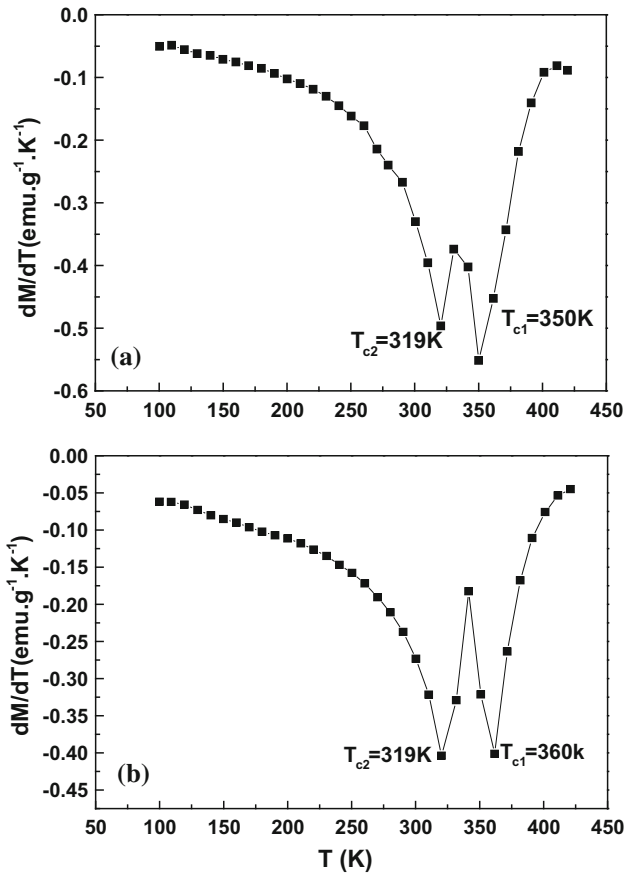

Fig. 9 dM/dT as function of temperature. (**a**) x = 0.025 and (**b**) x = 0.15

manganites can significantly influence the magnetic and transport properties of the compounds [28, 37, 38].

Comparing T_{ms} with T_C, we note that the value of T_{ms} is smaller and the variation is much larger. The PM–FM dominates by the LSMO grains, whereas the M-S transition is controlled by the grain boundary between LSMO grains. The large difference between T_C and T_{ms} can be attributed to the existence of magnetic disorder in the grain boundary region [39].

The differential of the magnetization, as shown in Fig. 9a and 9b, indicates the existence of second Curie temperature (T_{C2}) below the first T_{C1}. The value of this transition temperature is constant for all doping sample, as shown in Table 2 and it is not clear in the parent compound. So, we can say that this transition (T_{C2}) due to the ZrO_2 phase, while the first transition (T_{C1}) due to the LaSrMnO confirms the separation of ZrO_2 as observed in the XRD and SEM.

4. Conclusions

The composites of $(La_{0.7}Sr_{0.3}MnO_3)_{1-x}/(ZrO_2)_x$ (x = 0.0–0.150, step 0.025) have been fabricated. The magnetic and transport properties have been studied at different temperatures. The structural analysis confirms the coexistence of two phases in the composites and the ZrO_2 insulator is mainly segregated at grain boundaries of LSMO. The highest magnetoresistance at low and room temperature has been found for the composites $x = 0.10$. In addition to, the sample $Zr_x = 0.075$ achieves the highest value of T_{ms}, T_C and $N(E_f)$, whereas it has a smallest value of E_ρ, W_h and γ, due to a large Polarn formation. The magnetization measurements show the existence of two Curie temperatures, the first (T_{c1}) point to LSMO, while the second (T_{C2}) confirms ZrO_2 phase.

Acknowledgments Authors acknowledge the financial support provided by the Science and Technology Development Fund (STDF), Egypt, Grant Project No 3002.

References

[1] I El-Kassab, A M Ahmed, P Mandal, K Bearner, A Kattwinkel and U Sondermann *Phys. B* **305** 233 (2001)
[2] T Walter et al *Appl. Phys. Lett.* **74** 2218 (1999)
[3] X L Wang, S X Dou, H K Liu, M Ionescu and B Zeimetz *Appl. Phys. Lett.* **73** 396 (1998)
[4] L I Balcells, A E Carrillo, B Martinez and J Fontcuberta *Appl. Phys. Lett.* **74** 4014 (1999)
[5] O A Shlyakhtin, Y J Oh and Y D Tretyakov *Solid State Commun.* **117** 261 (2001)
[6] J M Liu et al. *Appl. Phys. Lett.* **78** 1110 (2001)
[7] S Gupta, R Ranjit, C Mitra, P Raychaudhuri and R Pinto *Appl. Phys. Lett.* **78** 362 (2001)
[8] A M Ahmed *Phys. B* **352** 330 (2004)
[9] A M Ahmed, S A Saleh, E M M Ibrahim and H F Mohamed *J. Magn. Magn. Mater.* **301** 452 (2006)
[10] A M Ahmed, A K Diab and H F Mohamed *J. Supercond. Nov. Magn.* **24** 597 (2011)
[11] B Huang, Y Liu, R Zhang, X Yuan, C Wang and L Mei *J. Phys. D: Appl. Phys.* **36** 1923 (2003)

[12] W J Lu, Y P Sun, X B Zhu, W H Song and J J Du *Mater. Lett.* **60** 3207 (2006)
[13] J B Torrance, P Lacorre and A I Nazzal *Phys. Rev. B* **45** 8209 (1992)
[14] I K Kamilov et al. *J. Exp. Theor. Phys.* **105** 774 (2007)
[15] K Bearner, P Mandal and R V Helmolt *Phys. stat. sol.* (b) **223** 811 (2001)
[16] A Banerjee, S Pal and B K Chaudhuri *J. Chem. Phys.* **115** 1550 (2001)
[17] L Pi, L Zheng and Y Zhang *Phys. Rev. B* **61** 8917 (2000)
[18] N F Mott *Metal Insulator Transitions* (London: Taylor and Francis) (1990)
[19] M Viret, L Ranno and J M D Coey *Phys. Rev. B* **55** 8067 (1997)
[20] N Mannella et al. *Phys. Rev. Lett.* **92** 166401 (2004)
[21] C H Sun et al. *J. Phys. Chem. Solids* **70** 286 (2009)
[22] A M Ahmed, H F Mohamed and M Soka *Low Temp. Phys.* **40** 418 (2014)
[23] I G Austin and N F Mott *Adv. Phys.* **18** 41(1969)
[24] G Venkataiah et al. *Phys. B* **357** 370 (2005)
[25] T Holstein *Ann. Phys. (NY)* **8** 343 (1959)
[26] N F Mott and E A Davis *Electronic Press in Non-Crystalline Materials* 2nd edn. (Oxford: Clarendon press) (2012)
[27] S Mollah, H L Huang, H D Yang, S Pal, S Taran and B K Chaudhurib *J. Magn. Magn. Mater.* **284** 383 (2004)
[28] A Maignan, C Martin and B Raveau *Z. Phys. B* **102** 19 (1997)
[29] C Kwon et al. *J. Appl. Phys.* **81** 4950 (1997)
[30] Y Sun, W Tong, X Xu and Y Zhang *J. Magn. Magn. Mater.* **231** 195 (2001)
[31] A-M Haghiri-Gosnet and J-P Renard *J. Phys. D: Appl. Phys.* **36** R127 (2003)
[32] A Gupta et al. *Phys. Rev. B* **54** 15629 (1996)
[33] H Y Hwang, S-W Cheong, N P Ong and B Batlogg *Phys. Rev. Lett.* **77** 2041 (1996)
[34] T Kimura, Y Tomioka, H Kuwahara, A Asamitsu, M Tamura and Y Tokura *Science* **274** 1698 (1996)
[35] N Mahamdioua, A Amira, S P Altintas, A Varilci and C Terzioglu *Phys. B* **429** 12 (2013)
[36] N Mahamdioua et al. *J. Supercond. Nov. Magn*. **26** 1441 (2013)
[37] B Raveau, C Martin and A Maignan *J. Alloy. Compd.* **275** 461 (1998)
[38] A I Coldea et al. *Phys. Rev. B* **65** 54402 (2002)
[39] L E Hueso, J Rivas, F Rivadulla and M A Lo'pez-Quintela *J. Appl. Phys*. **89** 1746 (2001)